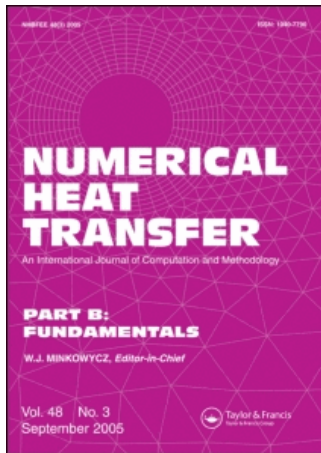


This article was downloaded by:[2007 Korea University - Seoul Campus]  
On: 16 December 2007  
Access Details: [subscription number 768980396]  
Publisher: Taylor & Francis  
Informa Ltd Registered in England and Wales Registered Number: 1072954  
Registered office: Mortimer House, 37-41 Mortimer Street, London W1T 3JH, UK



## Numerical Heat Transfer, Part B: Fundamentals

### An International Journal of Computation and Methodology

Publication details, including instructions for authors and subscription information:  
<http://www.informaworld.com/smpp/title~content=t713723316>

### Modeling Transport Phenomena of High Mass Loadings with Applications to Fire Suppression

David J. Glaze <sup>a</sup>; Sam S. Yoon <sup>b</sup>; John C. Hewson <sup>a</sup>; Paul E. DesJardin <sup>c</sup>

<sup>a</sup> Fire Science and Technologies, Sandia National Laboratories, Albuquerque, New Mexico, USA

<sup>b</sup> Department of Mechanical Engineering, Korea University, Anamdong, Sungbukgu, Seoul, South Korea

<sup>c</sup> Department of Mechanical & Aerospace Engineering, University at Buffalo, State

University of New York, New York, USA

Online Publication Date: 01 February 2008

To cite this Article: Glaze, David J., Yoon, Sam S., Hewson, John C. and DesJardin, Paul E. (2008) 'Modeling Transport Phenomena of High Mass Loadings with Applications to Fire Suppression', Numerical Heat Transfer, Part B: Fundamentals, 53:2, 118 - 142

To link to this article: DOI: 10.1080/10407790701702999

URL: <http://dx.doi.org/10.1080/10407790701702999>

PLEASE SCROLL DOWN FOR ARTICLE

Full terms and conditions of use: <http://www.informaworld.com/terms-and-conditions-of-access.pdf>

This article maybe used for research, teaching and private study purposes. Any substantial or systematic reproduction, re-distribution, re-selling, loan or sub-licensing, systematic supply or distribution in any form to anyone is expressly forbidden.

The publisher does not give any warranty express or implied or make any representation that the contents will be complete or accurate or up to date. The accuracy of any instructions, formulae and drug doses should be independently verified with primary sources. The publisher shall not be liable for any loss, actions, claims, proceedings, demand or costs or damages whatsoever or howsoever caused arising directly or indirectly in connection with or arising out of the use of this material.

## MODELING TRANSPORT PHENOMENA OF HIGH MASS LOADINGS WITH APPLICATIONS TO FIRE SUPPRESSION

David J. Glaze<sup>1</sup>, Sam S. Yoon<sup>2</sup>, John C. Hewson<sup>1</sup>,  
and Paul E. DesJardin<sup>3</sup>

<sup>1</sup>Fire Science and Technologies, Sandia National Laboratories, Albuquerque, New Mexico, USA

<sup>2</sup>Department of Mechanical Engineering, Korea University, Anamdong, Sungbukgu, Seoul, South Korea

<sup>3</sup>Department of Mechanical & Aerospace Engineering, University at Buffalo, State University of New York, New York, USA

*Improvements to the existing Eulerian-Lagrangian two-phase dilute spray model, referred to as Vulcan, are required in order to handle high mass loadings or very small solid particles. Such flows are relevant to modern fire-suppression techniques among other applications. These improvements include developing a new treatment for efficiently integrating small particles, a new subcycling time-step selection algorithm for the time-splitting solution technique, and a new treatment for placement of the two-way coupling source terms on the fluid grid. Despite the added complexity of these modifications, performance tuning of the code was also performed so that the solution speed is either equivalent to or faster than the previous code, depending on particle size. The new algorithms are applied to predicting suppressant distribution from a Goodrich-244 fire-suppression system in a simulated aircraft cargo bay. Results using these new algorithms indicate that the larger particles found in the Goodrich-244 suppressant disperse more uniformly throughout the aircraft cargo bay, although a large fraction of these particles adhere to the side walls before being delivered to the fire. Buoyancy of the hot combustion products was found to inhibit particle dispersion, and to generate large unwanted convective heat fluxes to the roof of the cargo bay.*

### INTRODUCTION

Fire suppression is one of many applications for which the transport of condensed phases is key. In traditional and advanced water-based suppression systems, the large latent heat of vaporization of water is a key factor in removing heat from and quenching fires. Another new approach to fire suppression, employed in the Goodrich-244 system described in this report, takes advantage of catalytic

Received 11 July 2006; accepted 18 August 2007.

Sandia National Laboratories (SNL) is a multiprogram laboratory operated by Sandia Corporation, a Lockheed Martin Company, for the United States Department of Energy's National Nuclear Security Administration under Contract DE-AC04-94AL85000. The second author acknowledges that this work was partially supported by a Korea Research Foundation Grant funded by the Korean Government (MOEHRD), KRF-2007-331-D00061.

Address correspondence to Sam Sukgoo Yoon, Department of Mechanical Engineering, Korea University, Anamdong, 5-Ga, Sungbukgu, Seoul, 136-713, Korea. E-mail: skyoon@korea.ac.kr



application is described in the application Sections. The other application of interest is the prediction of water spray evolution with relatively heavy mass loading. The application of the spray module to the water spray problem is described in detail in [2, 3]. Each of these applications has a high mass loading, and the particle size in the Goodrich-244 system is small enough that time-scale separation makes simulations intractable using the original algorithms [2].

## SPRAY TRANSPORT MODEL

Simulations were conducted using Sandia's Vulcan fire-physics code. The spray model is a recent addition to Vulcan [2], and additional capabilities are still in development. The following subsections detail some of the verifications and improvements made to the basic particle transport model, to assure its accuracy for the Goodrich-244 SPGG system simulations.

### Spray Model Methodology

Vulcan solves the Reynolds-averaged Navier-Stokes (RANS) equations, coupled with equations for species, temperature, and the turbulent kinetic energy and dissipation using well-known methods [4, 5]. In addition to the gas-phase species, condensed-phase particles are transported using a Lagrangian method coupled to the Eulerian grid. This particle transport model is derived from the stochastic separated-flow (SSF) model [2], and this is the same model used in the popular internal-combustion-engine simulation code, KIVA [6, 7]. The model employs parcels to represent a large number of individual particles (of the order of billions for extremely small particle sizes). These parcels are transported according to calculated force balances on individual particles, and the particle size and temperature are evolved according to mass and energy balances. A large number of such parcels (tens or hundreds of thousands) are tracked to describe the evolution of the condensed phase. Properties of particles, including their size, temperature, composition, and thermal properties such as specific heat, density, drag coefficients, etc., are assumed to be identical for all particles in a parcel. The parcels are transported by the mean flow and by turbulent fluctuations. Other comparable spray models are available in Wiedenhoefer and Reitz [8], Tolpadi et al. [9], Chow and Yao [10], Raju [11], Consalvi et al. [12], and Roychoudhary and Bergman [13].

When a particle collides with a solid wall, it is assumed to adhere to the wall if the impact velocity (kinetic energy) is sufficiently high, and bounces otherwise. In general, adherence is the predominant result of collisions for the particles considered here. It is well known that fine powders can be convectively lifted from surfaces and transported elsewhere, but this is beyond the scope of the current study. As such, it is expected that the present simulations will underestimate the particle spreading following wall impingement. Further details regarding the implementation of the SSF model are provided in [2].

### Unsteady Terms in Particle Transport Equations

When using the SSF model, the particle locations evolve according to a force balance, Newton's second law, with the resultant leading to particle acceleration [14].

The full particle momentum equation contains a number of terms that can be categorized as either a steady force or an unsteady force. The unsteady forces tend toward zero for a particle in a stationary flow field, but are still often small with respect to the steady forces in commonly encountered unsteady flows. For this reason, the unsteady terms are often safely neglected in particle simulations, since they can be complex and expensive to calculate. This is the assumption made in the present particle momentum formulation in the Vulcan spray module, where only the steady aerodynamic drag and gravitational body forces are modeled [2]. The validity of this assumption is assessed below for the type of particles encountered in the Goodrich-244 suppressant.

The full unsteady momentum equation for noncirculating and nondeforming spherical liquid or solid particles [15] is

$$m_p = \frac{du_{p_i}}{dt} = F_{D_i} + F_{P_i} + F_{A_i} + F_{H_i} + F_{L_i} + F_{B_i} \quad (1)$$

where  $m_p$  is the particle mass,  $u_{p_i}$  is the particle velocity, and  $t$  is time. The forces on the right-hand side of this equation are defined as

$$\begin{aligned} F_{D_i} &= \frac{\pi}{8} \rho_g D_p^2 C_D |u_{g_i} - u_{p_i}| (u_{g_i} - u_{p_i}) \quad (\text{aerodynamic drag}) \\ F_{P_i} &= \frac{\pi}{6} \rho_g D_p^3 \frac{Du_{g_i}}{Dt} \quad (\text{pressure gradient}) \\ F_{A_i} &= \frac{\pi}{6} C_A \rho_g D_p^3 \left( \frac{Du_{g_i}}{Dt} - \frac{du_{p_i}}{dt} \right) \quad (\text{added mass}) \\ F_{H_i} &= \frac{\pi}{4} C_H D_p^2 \sqrt{\frac{\rho_g \mu_g}{\pi}} \int_0^t \frac{d/d\tau (u_{g_i} - u_{p_i})}{\sqrt{t - \tau}} d\tau \quad (\text{history}) \\ F_{L_i} &= 2.72 D_p^2 \sqrt{\rho_g \mu_g} \frac{S_{ij}}{(S_{lk} S_{kl})^{1/4}} (u_{g_j} - u_{p_j}) \quad (\text{Saffman lift}) \\ F_{B_i} &= \frac{\pi}{6} D_p^3 (\rho_p - \rho_g) g_j \delta_{ij} \quad (\text{body force}) \end{aligned} \quad (2)$$

where  $\rho_g$ ,  $\mu_g$ , and  $u_{g_i}$  are the gas density, viscosity, and velocity, and  $\rho_p$ ,  $D_p$ , and  $u_{p_i}$  are the particle density, diameter, and velocity, respectively. Gravitational acceleration is represented by  $g_j$ , and the local carrier gas strain rate tensor is defined as  $S_{ij} = 1/2(\partial u_i/\partial x_j + \partial u_j/\partial x_i)$ . Additionally, the two substantial derivatives of the gas velocity in these expressions are defined as

$$\begin{aligned} \frac{Du_{g_i}}{Dt} &= \frac{\partial u_{g_i}}{\partial t} + u_{g_j} \frac{\partial u_{g_i}}{\partial x_j} \\ \frac{du_{g_i}}{dt} &= \frac{\partial u_{g_i}}{\partial t} + u_{p_j} \frac{\partial u_{g_i}}{\partial x_j} \end{aligned} \quad (3)$$

The original equation developed in [15] is only formally correct in the limit of zero particle Reynolds number,  $Re = \rho_g |u_{g_i} - u_{p_i}| D_p / \mu_g$ . The additional coefficients  $C_D$ ,  $C_A$ , and  $C_H$  in Eqs. (2) are added to adjust the respective terms for finite

Reynolds numbers [16]. The coefficients  $C_A$  and  $C_H$  are both generally  $O(1)$ , and are thus not considered in the present order analysis. The coefficient of drag  $C_D$ , however, can span many orders of magnitude. The Goodrich-244 suppressant consists primarily of micrometer-sized particles, for which typically  $Re_p \ll 1$ , so that the Stokes drag regime is a good approximation for the present analysis, reducing the coefficient of drag to the form  $C_D = 24/Re_p$  [17].

The force expressions in Eqs. (2) can be nondimensionalized by the mean particle and gas thermophysical properties as well as combinations of the particle diameter and slip velocity to obtain reference length, velocity, and time scales. Ratios with the drag force reveal the relative orders of magnitude for the various forces:

$$\begin{aligned}
 \frac{F_{P_j}}{F_{D_j}} &= O(Re_p) \quad (\text{pressure gradient}) \\
 \frac{F_{A_j}}{F_{D_j}} &= O(Re_p) \quad \text{added mass} \\
 \frac{F_{H_j}}{F_{D_j}} &= O(Re_p^{1/2}) \quad (\text{history}) \\
 \frac{F_{L_j}}{F_{D_j}} &= O(Re_p^{1/2}) \quad (\text{Saffman lift}) \\
 \frac{F_{B_j}}{F_{D_j}} &= O\left(\frac{Re \rho_p}{Fr \rho_g}\right) \quad (\text{body force})
 \end{aligned} \tag{4}$$

where the Froude number is defined in terms of reference quantities as  $Fr = u_{\text{ref}}^2/gD_p$ .

Previous experience indicates that the gravitational settling velocity of a particle in a quiescent environment is a good order estimate of the typical particle slip velocities experienced in a turbulent flow at moderate Reynolds numbers. For the Goodrich-244 suppressant, available information indicates that the particles range in size from about  $0.02 \mu\text{m}$  up to about  $100 \mu\text{m}$ , with the majority below  $40 \mu\text{m}$  [18]. The unsteady forces are more important for larger particles, so for a somewhat large  $15\text{-}\mu\text{m}$  spherical KBr particle with a density of  $2,300 \text{ kg/m}^3$ , the settling velocity is approximately  $15.3 \text{ mm/s}$ . This indicates a typical particle Reynolds number of about  $Re_p = 1.44 \times 10^{-2}$ .

Aerodynamic drag is usually the dominant force acting on a particle, so it must be retained in Eq. (1). Using the previous estimate of the particle Reynolds number, the order expressions in Eqs. (4) indicate that the gravitational body force will be  $O(10)$  with respect to aerodynamic drag, and thus cannot be neglected. The pressure gradient and added mass forces will be  $O(10^{-2})$  with respect to aerodynamic drag, and can usually be neglected if the additional constraint of  $\rho_p/\rho_g \gg 1$  is met [19, 20]. Since  $\rho_p/\rho_g = O(10^3)$  for the present work, these two forces can be neglected. The history force will typically be  $O(10^{-1})$  for the present simulations, and it can usually be neglected if either  $\rho_p/\rho_g > 500$  or  $\tau_v/\tau_f < 0.5$ , where  $\tau_v$  is the particle velocity relaxation time  $\tau_v \approx \rho_p D_p^2/18 \mu_g$  and  $\tau_f$  is a characteristic time scale of the fluid turbulence [21]. Although the order of magnitude for this force indicates that it

may not always be negligible, the density criterion is easily met. Since including this unsteady force in the particle momentum equation adds a significant cost and storage requirement, it will be neglected for the present work. The Saffman lift force will also be  $O(10^{-1})$  with respect to aerodynamic drag, but its magnitude may increase significantly in regions of both strong shear and a sustained particle slip velocity. The shear layer at the edges of the suppressant generator jets can create a large lift force, but since the particles are condensed directly from the gas in this region, they will likely not have a significant slip velocity. Thus, this force will also be neglected for the present study.

The overall result is that the existing model for aerodynamic drag and body force is sufficient for the Goodrich-244 SPGG simulations. Care should be taken, however, when simulating larger particles or particles with a density closer to that of the carrier gas, since some of the unsteady forces may become important to the particle behavior. Regardless, the steady forces alone will generally provide a good solution when only time-averaged particle behavior is measured. More information about these forces can be found in [20].

Available images of the Goodrich-244 KBr particles [18] indicate that many of the particles are generally cubic in shape, and so they will experience a larger aerodynamic drag than equivalent spherical particles. The existing drag coefficient model in the code assumes spherical particles, so a modification is necessary for the present work. Following the evaluation of available nonspherical correlations [22, 23], we use

$$\frac{C_D}{K_2} = \frac{24}{\text{Re}_p K_1 K_2} \left[ 1 + 0.1118(\text{Re}_p K_1 K_2)^{0.6567} \right] + \frac{0.4305}{1 + 3,305/\text{Re}_p K_1 K_2} \quad (5)$$

where  $K_1$  and  $K_2$  are defined for isometric particles as

$$K_1 = \frac{1}{\frac{1}{3} + \frac{2}{3}\psi^{-1/2}} \quad (6)$$

$$K_2 = 10^{1.8148(-\log_{10} \psi)^{0.5743}}$$

The variable  $\psi$  is the particle shape factor (also sometimes called the sphericity), defined as

$$\psi = \frac{A_{\text{sphere}}}{A_p} \quad (7)$$

where  $A_p$  is the surface area of the particle and  $A_{\text{sphere}}$  is the surface area of a sphere with the same volume. For the cubic particles considered here,  $\psi = 0.806$ .

## TWO-WAY COUPLING TREATMENTS

While testing the Vulcan spray module with the Goodrich-244 SPGG problem, some nonphysical temperature and velocity trends were identified in the results. While the first-generation code [2] worked well for simple problems with light particle mass loading, the heavy mass loading in this scenario revealed some

shortcomings in the selected mass, momentum, and energy coupling between the particles and the gas. These issues are magnified in the water spray described in [18], and that simulation will be used to document the developments described in this section.

### Subcycling Time-Step Prediction

The maximum stable time-step size for the particle ordinary differential equations (ODEs) is generally several orders of magnitude smaller than the time-step sizes selected for the Vulcan continuous-phase solution. To keep simulations affordable and to avoid the complexity and expense of a fully implicit solution, a time-splitting technique is used to advance the simulation [2]. This time-splitting algorithm works by freezing the solution of the gas phase while the particles are advanced through a number of time steps. Then, the cumulative effect of the particles over this time is used to update the gas, and this procedure is repeated until the particles are brought up to the current time level of the gas solution. Each of these time-splitting cycles is referred to as a subcycling time step. As the subcycling time step is made smaller, the solution becomes more accurate but also much more expensive. A subcycling time step that is too large can lead to severe inaccuracies or even simulation instability, despite a stable time-step size being used for the actual particle ODE advancement inside each subcycling step.

Figure 1 illustrates a possible scenario where large subcycling time steps can lead to simulation instability. For concreteness, say that the particles are initially at a velocity of 100 m/s, and they are introduced into a stationary gas. Say that the particle mass loading is such that the local long-time equilibrium velocity between the particles and the gas is 80 m/s. Assume that the particles are small enough that an almost complete equilibrium exists at the end of the gas-phase time step  $\Delta t_g$ , which is larger than the total time increment illustrated. In this example scenario, the particle subcycling time step  $\Delta t_p$  is initially selected to be too large. Due to the

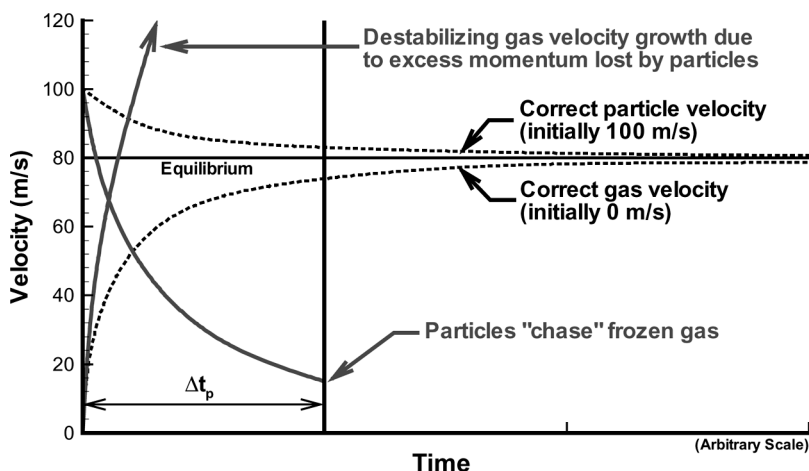


Figure 1. Example scenario requiring subcycling time-step control for stability.

time-splitting solution technique used, the gas velocity is not allowed to vary within each subcycling step. The gas velocity does not increase to meet the particle velocity during the step, resulting in the particles “chasing” the stationary gas velocity and overshooting the equilibrium. Once the particles have reached time  $\Delta t_p$ , their erroneous lost momentum is used to adjust the gas velocity, resulting in a drastic overshoot of the equilibrium. An even larger overshoot can occur during the next subcycling time step, because the particles will now be chasing the erroneously high gas velocity. Without special treatment, this behavior can cause the code to destabilize.

The prior methodology in the Vulcan spray module for handling extreme cases such as this (described in detail in [2]) involved estimating the maximum possible mass, momentum, and energy transfer to the gas and limiting the actual two-way coupling source terms to a fraction of this value. An initial guess was made for the initial step size, and if source-term clipping was required to keep the solution stable, the next subcycling time step size was then reduced. A lower limit was used to prevent the step size from becoming unreasonably small. The various code control parameters for the source-term clipping factors and minimum time step could usually be tuned to result in a stable solution, although the nonconservative nature of the source-term clipping and the strong nonlinearities in the problem could still yield an incorrect or unstable solution for challenging problems if not tuned properly.

Since the optimum values of the source-term clipping parameters are problem-dependent, it was decided to seek an alternative methodology that would be more robust and would guarantee an accurate and stable solution without additional input from the user. The general idea of the new methodology is to make a reasonable estimate of the maximum stable time step before each step is taken, thus eliminating the need for any source-term clipping. This would be a self-adjusting methodology that requires no additional input from the user.

Consider a single grid cell containing an arbitrary mixture of particles of different sizes, velocities, and thermophysical properties. A simple momentum balance between the particles and gas at an initial time and a final time identified as states (1) and (2), respectively, is

$$\underline{u}_{g,2} = \frac{1}{\rho_g V_{\text{cell}} \phi} \left[ \rho_g \underline{u}_{g,1} V_{\text{cell}} \phi - \sum_{N_p} m_p (\underline{u}_{p,2} - \underline{u}_{p,1}) \right] \quad (8)$$

where  $\phi$  is the particle void fraction in the grid cell and  $V_{\text{cell}}$  is the cell volume. The summation is over all  $N_p$  particles in the cell. This expression represents the final gas velocity in the cell, given a change in particle velocities  $\underline{u}_{p,2}$ . An estimate of this particle velocity difference can be obtained from a linearized form of the particle momentum equation, Eq. (1), including only the dominant drag force:

$$\frac{d\underline{u}_p}{dt} = \frac{(\underline{u}_{g,1} - \underline{u}_p)}{\tau_v} \quad (9)$$

where  $\tau_v$  is the particle velocity relaxation time, assumed constant and approximated from particle properties at time (1) by

$$\tau_v = \frac{\rho_p D_p^2}{18\mu_g} \left( \frac{24}{C_D \text{Re}_p} \right) \quad (10)$$

Note that, in these expressions, the initial gas velocity is assumed constant. Since the time-splitting integration technique used in the code makes the same assumption of a constant gas velocity over each subcycling time step, this is a good approximation for the actual particle behavior in the simulation. Integrating Eq. (9) between time (1) and time (2) with  $\Delta t_p = t_2 - t_1$  yields an estimate of the final particle velocity:

$$\underline{u}_{p,2} = \underline{u}_{g,1} - (\underline{u}_{g,1} - \underline{u}_{p,1})e^{-\Delta t_p/\tau_v} \quad (11)$$

Substituting this into Eq. (8) yields an estimate of the final gas velocity at the end of the subcycling time step based only on the known initial conditions:

$$\underline{u}_{g,2}^{\text{est}} = \underline{u}_{g,1} + \frac{1}{\rho_g V_{\text{cell}} \phi} \sum_{N_p} m_p (\underline{u}_{p,1} - \underline{u}_{g,1}) (1 - e^{-\Delta t_p/\tau_v}) \quad (12)$$

This velocity estimate is not enough to select an appropriate subcycling time step, however. A realizability condition is also needed for the velocity to ensure that the selected time step will not drive the final gas velocity beyond that which is physically achievable in a realistic environment. Unfortunately, a clear choice for this limit velocity is not readily available.

One possibility is to use an average particle velocity as a limit on the gas velocity, similar to the condition used previously in the spray module to calculate the source-term clipping factors. This choice could fail in the specific case of large, fast-moving particles, where the large size indicates a relatively slow momentum transfer to the gas for the given total particle mass. Simply using an average particle velocity would allow a change much larger than would actually occur, possibly resulting in stability problems.

Another possible choice is the long-time equilibrium velocity, illustrated schematically in Figure 1. This would be represented by

$$\underline{u}_{\text{eq}} = \frac{\rho_g \underline{u}_{g,1} V_{\text{cell}} \phi + \sum_{N_p} m_p \underline{u}_{p,1}}{\rho_g V_{\text{cell}} \phi + \sum_{N_p} m_p} \quad (13)$$

while this would be a good choice for most cases, it would fail in the particular case of a mixture of particles with a large variation of sizes and velocities. The long-time equilibrium would favor the larger, more massive particles, while the actual short-term behavior would favor the smaller particles, with a shorter velocity relaxation time. The short-term behavior is dominant for prediction of the subcycling time step.

To eliminate this limitation, a heuristic expression based on Eq. (13) is used that weights the momentum contribution of each particle based on the rate at which it can transfer momentum to the gas. This rate is approximated by  $m_p (d\underline{u}_p/dt)$ , so that the gas limit velocity can be expressed as

$$\underline{u}_{g,2}^{\text{lim}} = \frac{\rho_g \underline{u}_{g,1} V_{\text{cell}} \phi + \frac{N_p \sum_{N_p} m_p \underline{u}_{p,1} (m_p |u_{g,1} - u_{p,1}| / \tau_v)}{\sum_{N_p} m_p |u_{g,1} - u_{p,1}| / \tau_v}}{\rho_g V_{\text{cell}} \phi + \frac{N_p \sum_{N_p} m_p (m_p |u_{g,1} - u_{p,1}| / \tau_v)}{\sum_{N_p} m_p |u_{g,1} - u_{p,1}| / \tau_v}} \quad (14)$$

This new time-step selection procedure operates by first initializing the subcycling time step  $\Delta t_{\text{sub}}$  as that of the gas phase,  $\Delta t_g$ . Then, at the beginning of each subcycling time step, the following steps are executed:

1. Increase the current  $\Delta t_{\text{sub}}$  by a small fraction (currently 10% in the code) to improve affordability of the simulation.
2. The limit velocity is calculated with Eq. (14).
3. Using the current  $\Delta t_{\text{sub}}$  and the current gas and particle state, the final gas velocity is predicted with Eq. (12).
4. If the predicted change is beyond the limit, reduce  $\Delta t_{\text{sub}}$  by a small fraction (currently 10% in the code) and return to step 3. If not, the current subcycling time step is safe to use. Return to the particle calculation.

Note that the prediction and limit velocity are only crude estimates of the actual values, which can only be obtained exactly by a complete solution of the problem. The shortcomings of these expressions become more significant when only a very small change in the gas velocity will occur, as in a near-equilibrium condition. Small errors can lead to an unreasonable reduction in the predicted time step or even nonsensical results, as when the predicted velocity and the limit velocity are in opposite directions from the initial gas velocity. To prevent these types of problems, the current subcycling time step is assumed to be acceptable when the predicted change in the gas velocity is less than 10% of the local velocity magnitude.

For additional accuracy and an enhanced stability guarantee, a fraction of the maximum stable subcycling time step can be used. Early tests indicate that the time-step selection criterion detailed above is already conservative. No noticeable gains were achieved by further reducing the step size, so the predicted subcycling time step size is used unmodified. Note that the actual particle time step,  $\Delta t_p$ , is calculated as the minimum of a number of step sizes based on several physical criteria such as the cell crossing time and the turbulent eddy interaction time, of which  $\Delta t_{\text{sub}}$  is only one. See [2] for more information.

The present subcycling time-step selection methodology considers only the particle momentum equation and does not account for limitations imposed by energy and mass transfer. Tests indicate that the spray module runs well for most cases with the subcycling step size based only on momentum. Situations can be envisioned where this will not be the case, such as with stationary reacting or evaporating particles. Future development of the spray module should include a check for these additional constraints, although the theory outlined above may lead to an overly complex or expensive calculation and alternative techniques may need to be developed.

### Conservative Source Term Formulation

In a two-way coupled simulation, the particles affect the carrier gas through a set of source terms for mass, momentum, and energy transfer to the continuous-phase Navier-Stokes equations [2]. The previous formulation of these source terms was changed to make the coupling fully conservative.

The spray module had previously estimated the source terms based on the rate of change of particle mass, momentum, and energy at the end of each subcycling time step, as detailed in [2]. As an example, the nonevaporating portion of the momentum source term is estimated by  $-1/V_{\text{cell}} \sum_{N_p} F_{D_i}$ , where  $F_{D_i} = m_p(du_{p_i}/dt)$ . The velocity derivative at the end of the subcycling time step is illustrated schematically by the lower dotted line in Figure 2 that is tangent to the velocity curve.

What is actually desired is an estimate of the total momentum change of the particles over the subcycling time step, expressed in rate form. This can be determined from just the beginning and ending points of the curve in Figure 2, as illustrated by the upper dotted line. In fact, when using such a formulation, it is no longer necessary to segregate the source terms into evaporating and nonevaporating contributions. The new mass, momentum, and energy source terms are

$$\begin{aligned} S_{\text{mass}} &= -\frac{1}{V_{\text{cell}}} \sum_{N_p} \frac{\Delta m_p}{\Delta t_p} \\ S_{\text{mom},j} &= -\frac{1}{V_{\text{cell}}} \sum_{N_p} \frac{\Delta(m_p u_{p_j})}{\Delta t_p} \\ S_{\text{energy}} &= -\frac{1}{V_{\text{cell}}} \sum_{N_p} \frac{\Delta(m_p h_{p,l})}{\Delta t_p} \end{aligned} \quad (15)$$

where  $h_{p,l}$  is the enthalpy of the particle liquid (or solid). To be consistent with the reference temperature used for enthalpy calculation in the Vulcan code, the liquid enthalpy  $h_{p,l}$  is calculated as  $h_{p,l} = h_{p,g} - h_{p,lg}$ , where  $h_{p,g}$  is the enthalpy of the gaseous particle species at the same temperature and  $h_{p,lg}$  is the particle enthalpy of vaporization. The gaseous enthalpy  $h_{p,g}$  is calculated from existing Vulcan subroutines.

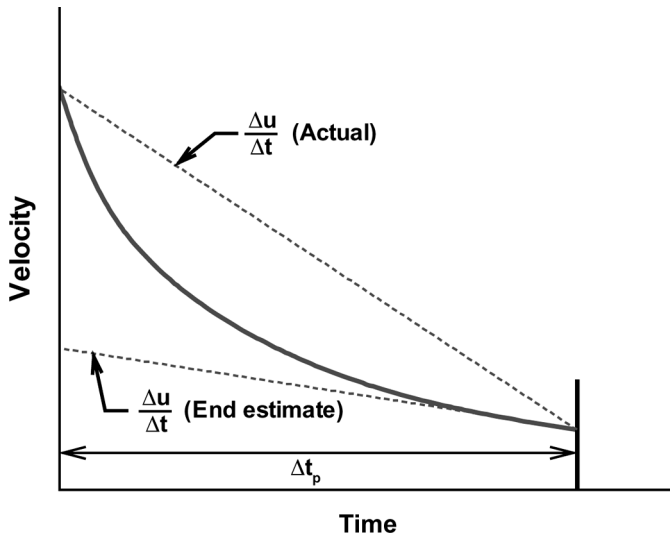


Figure 2. Two-way coupling momentum source term estimation.

### Source Term Localization

The modification to the formulation described in the previous two subsections increased the consistency and robustness of the code and reduced the magnitude of the stability problems described at the beginning of the two-way coupling treatment section.

Close inspection of the solution behavior indicated that the primary cause of the observed instability was the localization of the two-way coupling source terms onto the Vulcan grid. Figure 3 illustrates a possible circumstance where the localization error can cause an overprediction of the gas velocity. A single row of grid cells is considered for simplicity, illustrated along with the staggered grid for velocity storage at the bottom of the figure. The variable values are stored at the center of the corresponding grid cell. The “initial velocity” curve is the velocity stored at the center of the staggered grid cells, representing a sharp transition from 100 m/s to 0 m/s, as might occur at the leading edge of a developing spray. A small cloud of particles with a very heavy mass loading is moving at 100 m/s and is located on the grid as illustrated.

Physically, what should happen is the local gas will speed up to 100 m/s, while the particle velocity will drop slightly. In the simulation, the particles begin by interpolating a local gas velocity of about 50 m/s. After the particle calculations, a source term is generated that will act to increase the gas velocity toward 100 m/s. The existing spray module would then adjust the velocity in each staggered grid cell based on an average of the source terms contained in the fluid grid cells at either edge of the staggered cell. This, in effect, would increase the velocity both in front of and behind the particles. This process ends when the particles interpolate a gas velocity equal to their own velocity, which occurs at the stage labeled “Final Velocity” in Figure 3.

Notice that the peak final velocity is about 150 m/s for this scenario, although there is no physical mechanism in place that can raise the gas velocity beyond 100 m/s. Although it is not illustrated, similar behavior could occur with

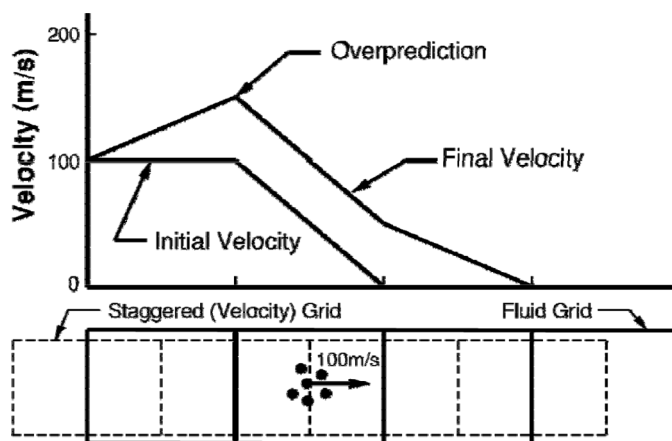


Figure 3. Momentum source term localization error demonstration.

neighboring rows of grid cells if this cluster of particles were off-center in the illustrated row. The particles will use a gas velocity that is linearly interpolated from the surrounding octant of grid cells, but the source term affects only a maximum of two of the eight cells, depending on the particle position. Both of these situations, combined with the previous time-stepping technique and source term formulation, would lead to unbounded velocity and temperature growth at the leading edge of the water-spray simulation.

An illustration of such an overshoot is shown in Figure 4, where the spray nozzle is located at the  $(0, 0, 0)$  coordinate location and is injecting water droplets in the positive  $X$  direction with a distribution of velocities that peaks at 100 m/s. The leading edge of the spray cloud accelerates up to more than two times the initial velocity, and the acceleration is concentrated in a single axial row of grid cells. With the changes described in the previous two subsections, this simulation is now stable.

A simple, inexpensive fix for the remaining source-term localization problem involves only applying the source terms to the grid cells containing the particles and using only the gas-phase properties of that cell for the particle calculations. No property interpolation is performed. This way, the particles affect only the grid cells that contributed to their behavior. With this simple zeroth-order interpolation technique, however, the particles experience a nonphysical step change in properties when crossing the grid boundaries. For this reason, this technique is undesirable.

Despite being somewhat nonphysical, this localization method does indeed prevent the overshoot problem. Rerunning the water-spray simulation with this localization technique for all source terms produces results that are much more physically satisfying, as shown in Figure 5. With this fix in place, the particles slow down upon injection into the stationary air, rather than speeding up. Although it is not shown, the particle and gas temperature drops slightly due to evaporation, as it should. Prior simulations resulted in a strong nonphysical droplet heating that did not end until either the particle completely evaporated or the maximum supported temperature (3,000 K) was reached in the Vulcan enthalpy lookup table.

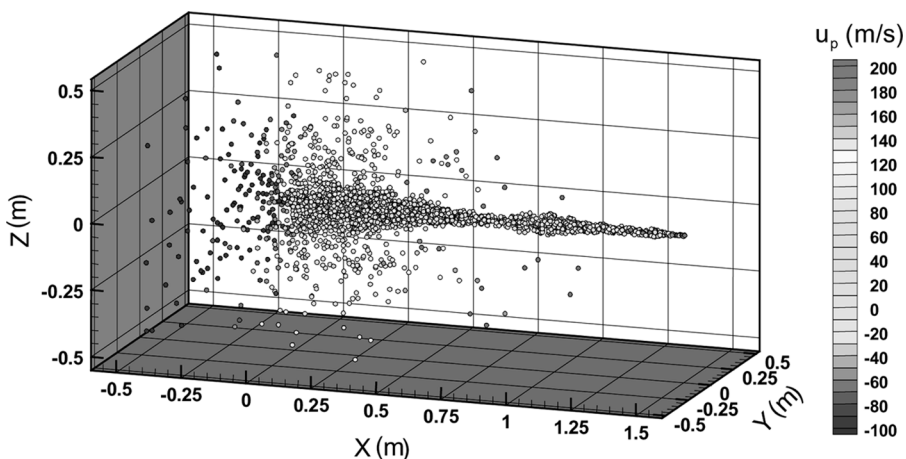


**Figure 4.** Velocity overshoot in water-spray simulation at  $t = 0.02$  s due to source-term localization errors.

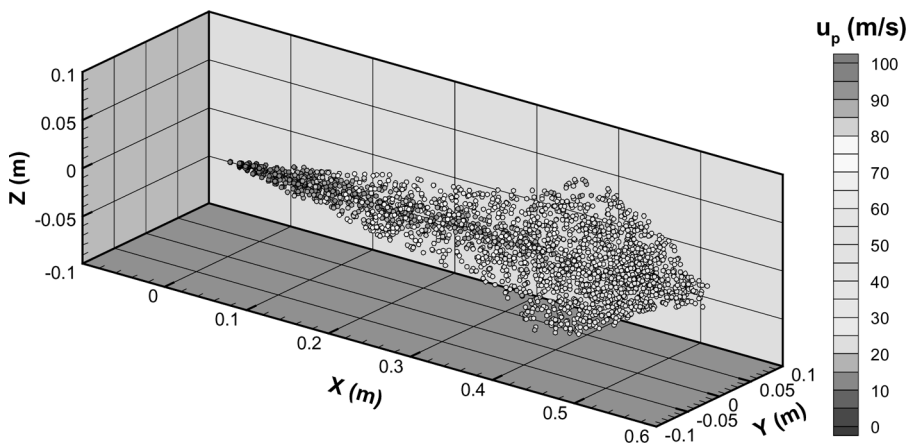


Figure 5. Water-spray simulation at  $t = 0.011$  s using zeroth-order source term localization.

Unfortunately, close inspection of the particle trajectories indicates some nonphysical behavior. A view normal to the  $X$ - $Z$  plane of this simulation is shown in Figure 6. Here, the particles can be seen to migrate away from the  $X$ - $Y$  plane passing through the spray centerline. A similar behavior occurs with the  $X$ - $Z$  plane. This trend becomes more exaggerated at later times in the simulation, and so is undesirable. The lack of interpolation of the gas thermophysical properties near these symmetry planes is the cause of this behavior, so an alternative technique is sought to prevent overshoot while still interpolating the gas properties.

The essence of the original source-term localization problem was that the source terms generated were not applied to all grid cells that were used to interpolate properties to the particle position, and those that received the source terms were sometimes driven to nonphysical conditions. The application of the source terms to these cells in a consistent manner is not straightforward, however. Figure 7 illustrates a particle surrounded by the eight grid cell centers used to interpolate the gas properties. This octant may represent either the fluid grid or any of the staggered velocity grids, depending on the variable being interpolated.

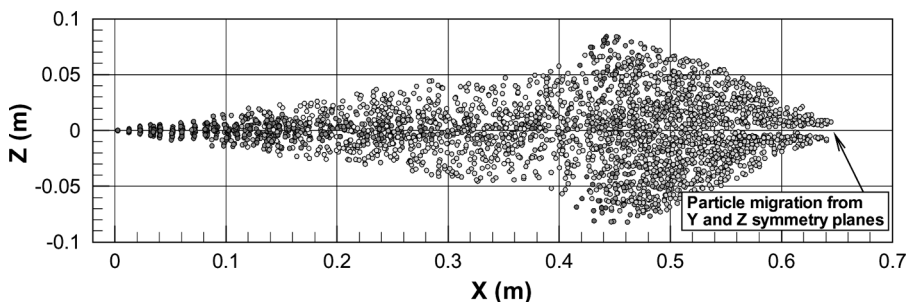


Figure 6. Illustration of particle migration away from  $Y$  and  $Z$  symmetry planes when using zeroth-order source term localization.

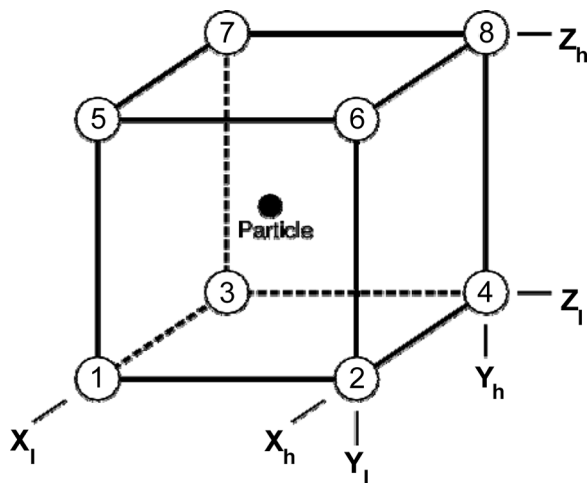


Figure 7. Interpolation octant for source term localization.

The source term distribution among these eight cells should depend on several factors. The first, and most obvious, is a spatial dependence. If a particle is exactly centered on one of the interpolation points, all of its source term should go to that cell, and if it is centered in the interpolation octant, the source term should be evenly distributed. Besides this geometric dependence, the source term localization should also depend on the gas thermophysical properties at each interpolation point. For instance, if seven of the eight corners have the same velocity as the particle while one corner is different, the source term generated will be in response solely to that one corner and the resulting source term should be biased toward this corner. A final constraint should also be placed on the source term so that it does not drive the gas property beyond that which is physically justifiable.

A new source-term localization technique is now developed which models the geometric and property dependencies described above. For momentum, a source term “affinity” is calculated for each of the eight interpolation octant corners. This is essentially the fraction of the source term in the octant that will be driven to that corner. The source term affinities are calculated as

$$A_{u_i,1} = \frac{A_{u_i,1}^*}{\sum_{n=1}^8 A_{u_i,n}^*}, \quad A_{u_i,2} = \frac{A_{u_i,2}^*}{\sum_{n=1}^8 A_{u_i,n}^*}, \dots, \quad A_{u_i,8} = \frac{A_{u_i,8}^*}{\sum_{n=1}^8 A_{u_i,n}^*} \quad (16)$$

where the raw components for each corner are

$$\begin{aligned} A_{u_i,1}^* &= \left( \frac{x_h - x_p}{x_h - x_l} \right) \left( \frac{y_h - y_p}{y_h - y_l} \right) \left( \frac{z_h - z_p}{z_h - z_l} \right) \text{MAX} \left[ \frac{S_{u_i}}{|S_{u_i}|} (u_{p_i} - u_{g_i}|_1), 0 \right] \\ A_{u_i,2}^* &= \left( \frac{x_p - x_l}{x_h - x_l} \right) \left( \frac{y_h - y_p}{y_h - y_l} \right) \left( \frac{z_h - z_p}{z_h - z_l} \right) \text{MAX} \left[ \frac{S_{u_i}}{|S_{u_i}|} (u_{p_i} - u_{g_i}|_2), 0 \right] \\ &\vdots \\ A_{u_i,8}^* &= \left( \frac{x_p - x_l}{x_h - x_l} \right) \left( \frac{y_p - y_l}{y_h - y_l} \right) \left( \frac{z_p - z_l}{z_h - z_l} \right) \text{MAX} \left[ \frac{S_{u_i}}{|S_{u_i}|} (u_{p_i} - u_{g_i}|_8), 0 \right] \end{aligned} \quad (17)$$

The first three terms in these expressions are the geometric scaling factors, and the last term is the property scaling factor. The velocity difference in the property scaling factors come from the observation that for low to moderate particle Reynolds numbers, the momentum source term is essentially linear in the slip velocity. This provides a simple scaling factor to weight the influence of each corner of the interpolation octant. The factor  $S_{u_i}/|S_{u_i}|$  is present to determine the sign of the source term which, when combined with the MAX( ) operator, locally shuts off the source term to prevent overshoot.

The development up to this point has been for the special case of a single particle. In actuality, the code simulates parcels of particles with identical properties [2]. For large parcels that cover many grid cells, a slightly different treatment is necessary. Due to turbulent diffusion, the particle parcels will grow in size with time. After a length of time has passed, most particles will approach an equilibrium state with the carrier gas. Not only will the source term magnitude be greatly reduced, it will be distributed to many grid cells, including all cells in the interpolation octant. Thus, the need to redistribute the source term in the interpolation octant is greatly reduced for large parcels.

To handle the simulation of parcels of particles, the fraction of the total parcel source term that belongs in the interpolation octant is first estimated by

$$f_{\text{oct}} = \frac{N_p|_{\text{oct}}}{N_p|_{\text{parcel}}} \tag{18}$$

where  $N_p|_{\text{oct}}$  is the number of particles in the octant of grid cells and  $N_p|_{\text{parcel}}$  is the total number of particles in the parcel. The local particle concentration for each cell is calculated using the normal distribution as described in [2]. The fraction of the source term that will be placed in the octant is then

$$S_{u_i}|_{\text{oct}} = f_{\text{oct}} S_{u_i} \tag{19}$$

Of this amount of source term in the octant, a fraction will be redistributed according to the source term affinity of each corner. The fraction is adjusted according to the size of the parcel. For each octant cell, the source term is then

$$S_{u_i}|_n = f_R A_{u_i,n} S_{u_i}|_{\text{oct}} + (1 - f_R) \frac{N_p|_n}{N_p|_{\text{parcel}}} S_{u_i} \tag{20}$$

where the redistribution weighting factor is

$$f_R = \frac{1 + f_{\text{oct}}}{2} \tag{21}$$

This has the effect that, if the parcel is very small, all of the source term in the octant is redistributed according to the affinities. If the parcel is very large, half of the octant source term is redistributed while the other half is placed in the octant according to the normal distribution. This way, the source term is still globally placed on the grid according to the normal distribution, while a fraction is redistributed in

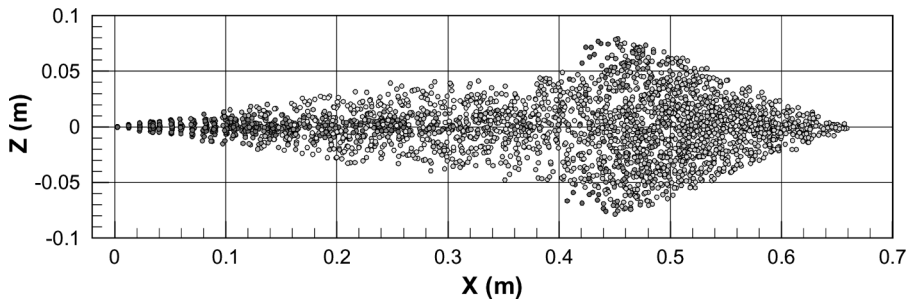


Figure 8. Water-jet simulation using new momentum source term localization.

the octant to prevent any rare destabilizing events. All cells outside the octant will always get a fraction of the source term according to the normal distribution.

Figure 8 shows the water-jet simulation at  $t = 0.01$  s using this new localization technique for the momentum source terms. Results are qualitatively very similar to those using zeroth-order interpolation, previously illustrated in Figure 6, except that the particles are no longer migrating away from the  $Y$  and  $Z$  symmetry planes of the jet. Unfortunately, this technique is quite expensive. Localizing the momentum source terms using this new technique adds about 30% to the execution time of the spray module. As such, the zeroth-order localization technique is still used for mass and energy, where no such artifacts as those illustrated in Figure 6 were observed. The zeroth-order localization code for momentum is still contained in the spray module, and a switch back to this technique can be made with little effort if the cost penalty is ever deemed unacceptable.

## APPLICATION TO THE GOODRICH-244 FIRE-SUPPRESSION SYSTEM

The modifications to the Vulcan spray module described in the previous sections allowed accurate and efficient simulation of the transient Goodrich-244 SPGG suppressant distribution. The following subsections detail the simulations performed with this model and some of the results.

### Simulation Configuration

The Goodrich-244 configuration under investigation consists of a dual-slot SPGG system mounted on the ceiling of an aircraft cargo bay mockup as shown schematically in Figure 9. This is similar to the compartment geometry in which aircraft cargo bay suppression systems are certified except for the fact that the upward taper found in the lower sections is neglected. The overall physical dimensions are  $10\text{ m} \times 3.7\text{ m} \times 1.65\text{ m}$ , and a computational grid resolution of  $120 \times 30 \times 30$  is employed. The grid was somewhat refined around the SPGG injector slots to improve the solution resolution in this area of sharp gradients. The SPGG system is mounted toward one end of the bay and off-center in the direction of the door.

The total mass flux from the generator is approximately  $0.091\text{ kg/s}$  ( $2\text{ lb/s}$ ), based on estimates of burning rate from Goodrich/UPCO [18]. The temperature

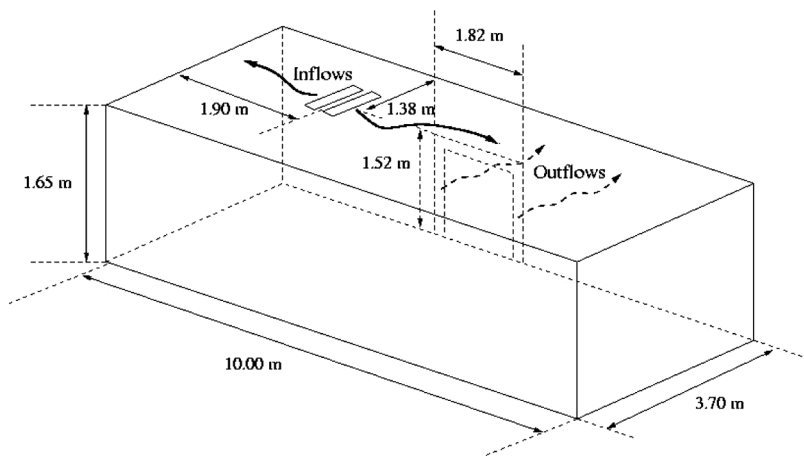


Figure 9. Model DC-10 cargo bay.

of the suppressant is assumed to be 1,200 K at the exit plane of the injector. The suppressant composition at the injector exit was also determined from information provided by Goodrich/UPCO personnel [18].

Given the mass burning rate of the propellant and the mixture composition, the mass flow rate of gaseous products from the generator will be 0.029 kg/s, while that of the particulates will be 0.062 kg/s. Given the temperature and assuming a pressure of 1 bar, the gaseous product exit velocity can be estimated from the ideal gas law. With a total generator slot cross-sectional area of  $3.23 \times 10^{-3} \text{ m}^2$  and neglecting velocity nonuniformities in the gas stream, the mean outflow velocity is estimated to be 14.8 m/s. The mass flow rates and generator slot area are divided between a pair of slots as shown in Figure 10. Injection ends after 10 s, when the initial 2 lb of propellant are consumed. Outflow to maintain a constant chamber pressure is through an array of openings centered on one wall to simulate leakage around a cargo door. Inlet air flow from airframe leakage was neglected, so the only inflow is from the SPGG system.

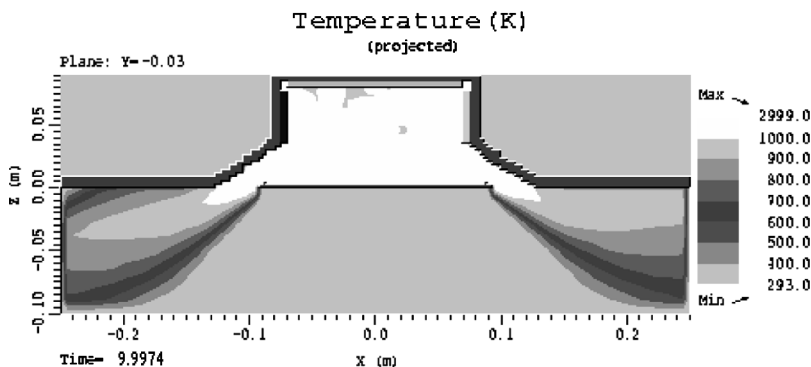


Figure 10. Simulation of SPGG injector cross section showing temperature contours near injection slots.

Additional initial conditions have been taken from correspondence with Goodrich representatives and the related report [1, 18]. The fire suppressant leaves the propellant injector through a pair of slots that are positioned so that the effluent tends to flow out (away from the adjacent slot) more than down. To obtain some estimates of the angle at which the flow should leave the slots, a series of numerical simulations of the propellant injector were conducted. In these simulations the particles were neglected so that only the gas-phase transport was considered. This approach was motivated by the nature of the particle formation; the particles are assumed to condense out of the gas-phase products at some point downstream of the actual propellant combustion. The propellant combustion is not modeled directly, but rather is represented by a mass source term on the top and two side surfaces nearest the slots, to mimic the actual placement of the solid propellant.

Figure 10 shows the flow pattern in and near the injector as predicted using Vulcan. Because the products of propellant combustion are hot (1,200 K), buoyancy and the Coanda effect (also known as “boundary-layer attachment”) cause the suppressant to flow along the ceiling. Prior to being moved toward the ceiling, the flow exits at an angle of roughly  $35^\circ$  below the horizontal plane. The injector is modeled as a pair of slots. Based on these detailed results, the initial mean flow direction for both the gas and particle mixture at the injector exit slots are set to  $35^\circ$  below horizontal, with the initial direction for each individual parcel allowed to vary plus or minus  $10^\circ$  to simulate the initial spread of particles across the gas flow.

It is well known that the degree to which particles follow the flow, as opposed to having ballistic trajectories, is strongly dependent on their size [24]. Smaller particles approach kinematic and thermodynamic equilibrium with the carrier gas more rapidly. Therefore, it was decided to study the effects of particle size on their transport properties throughout the model aircraft cargo bay, since delivery of the suppressant particles to the fire is critical to their effectiveness.

Of the dominant modes in the particle size distribution, particles with diameters of 2 and  $15\ \mu\text{m}$  were selected for investigation due to their unique behavior. Trial simulation results indicate that the  $2\text{-}\mu\text{m}$  particles have velocity and temperature relaxation times of the order of  $10^{-5}\text{ s}$  while the  $15\ \mu\text{m}$  particles have velocity and temperature relaxation times of the order of  $10^{-3}\text{ s}$ . With Vulcan gas-phase time steps of the order of  $10^{-3}\text{ s}$ , the smaller particles will generally be treated with the equilibrium method while the larger particles will be treated with the standard SSF model, described in the spray transport model section.

With a fixed mass flux, the number of particles injected is inversely proportional to the cube of the diameter, so approximately 422 times as many  $2\text{-}\mu\text{m}$  particles will be injected as  $15\text{-}\mu\text{m}$  particles. The total particle surface area is of interest in determining the surface catalytic effect for fire suppression. The surface area per particle is proportional to the square of the diameter, so after including the effect of different number densities, the total surface area is larger for the smaller particles by a factor of the diameter ratio (7.5). The particle density and temperature are taken to be  $2,300\text{ kg/m}^3$  and  $1,200\text{ K}$ , respectively, and particle evaporation is neglected, which is consistent with the actual KBr physics of the experiment.

### Fire-Suppressant Distribution

Fire suppression occurs through the joint effect of the particulate and the product gases ( $\text{CO}_2$ ,  $\text{H}_2\text{O}$ , and  $\text{N}_2$ ). These gases are transported throughout the cargo bay by the mean flow and the turbulent mixing. The distribution of  $\text{CO}_2$  along the injector plane at the end of injection is shown in Figure 11 as a representation of the overall product gas distribution. The association of the  $\text{CO}_2$  and other product gases with high temperatures causes the highest concentrations of these gases to remain near the cargo bay ceiling, due to buoyancy effects, and likely far from any potential fires along the floor of the cargo bay.

The particle transport model described in [2] allows prediction of the particle number density evolution in the cargo bay and the evolution of the particle surface area. The particle surface area is indicative of the surface available for chemical reactions to occur that might play a role in suppressing flame chemistry. Figure 12 shows the time evolution of surfaces of constant particle number density per volume for both the 2- $\mu\text{m}$  and 15- $\mu\text{m}$  particles. Because the mass flux of particles is fixed by the propellant burn rate, the particle number density is inversely proportional to the particle mass. This feature results in higher number density coverage for the smaller 2- $\mu\text{m}$  particles. The distribution of the number density at the end of the injection can also be viewed in a cross section of the cargo bay through the centerline of the SPGG injector in Figure 13.

In addition to affecting the number density, the momentum associated with differing particle sizes affects the wall-adhesion behavior and the subsequent particle dispersion. In both simulations, a high-velocity mixture of gas and particles impinges on the wall nearest the injector. The gas is forced to turn downward, away from the ceiling. The smaller particles are generally able to follow this motion, while many of the larger particles are unable to complete the turn before impinging on the wall. As is visible in Figures 12 and 13, a greater number of the 15- $\mu\text{m}$  particles adhere to the wall and are no longer transported to a potential fire in the cargo bay.

It is also observed in Figure 13 that the distribution of 15- $\mu\text{m}$  particles is more uniform over a particle number density range of  $1 \times 10^8$  to  $1 \times 10^{10}$  particles/ $\text{m}^3$  than the distribution of 2- $\mu\text{m}$  particles. Conversely, there are regions of significantly higher number density, exceeding  $1 \times 10^{12}$  particles/ $\text{m}^3$  in the distribution of 2- $\mu\text{m}$  particles. The greater uniformity for larger particles arises from the effect of particle momentum in enhancing dispersion. In turbulent flows, particles experience intermittent

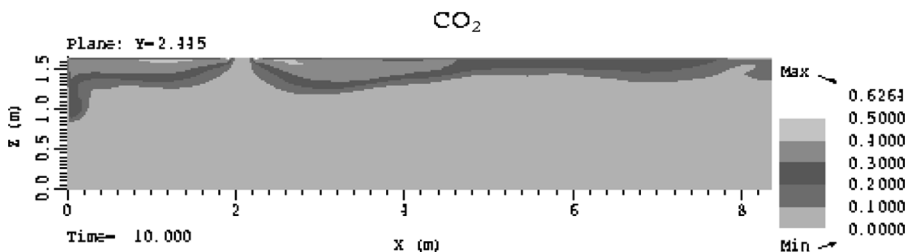


**Figure 11.**  $\text{CO}_2$  mole fraction in the cargo bay at a plane through the SPGG injector centerline at the end of injection (10 s) for 2- $\mu\text{m}$  particles.

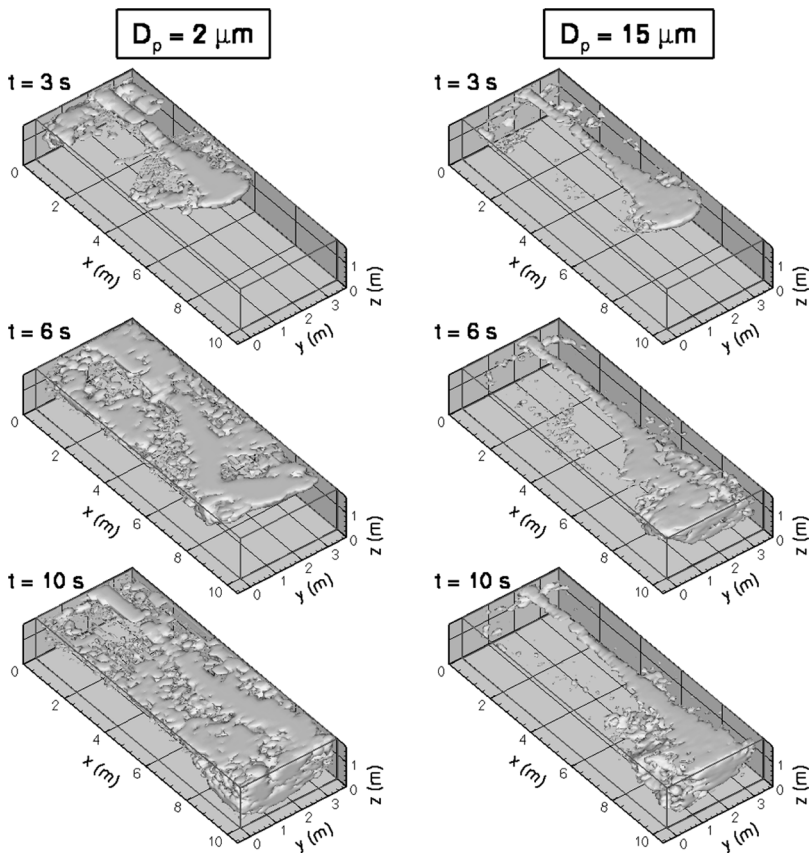


Figure 12. Particle number density iso-surface at  $1 \times 10^{10}$  particles/m<sup>3</sup>.

acceleration in random directions due to turbulent fluctuations. With turbulent mixing time scales of the order of tenths of seconds and particle velocity relaxation times of  $10^{-5}$  and  $10^{-3}$  s for the 2- and 15- $\mu\text{m}$  particles, respectively, the particles

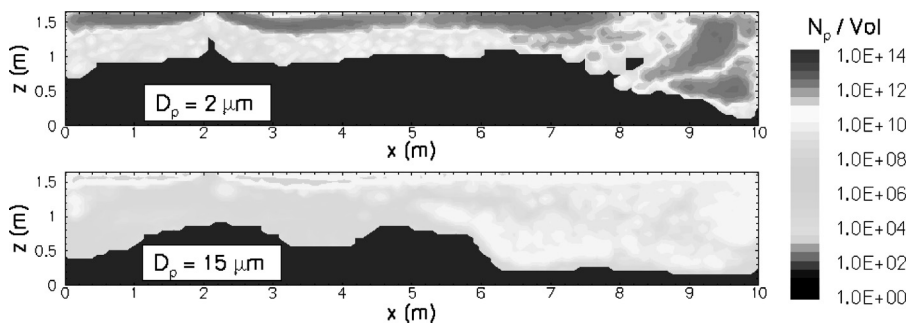


Figure 13. Particle number density in the cargo bay at the plane through the SPGG injector centerline at the end of injection (10 s).

are easily accelerated by turbulent fluctuations. Due to their momentum, the larger particles are able to maintain their fluctuation velocities for a longer time, leading to their enhanced dispersion.

Note, however, that significantly larger particles than those studied here would have sufficient inertia that they are not easily dispersed by turbulent fluctuations; dispersion is not monotonic in particle size and is optimized when the velocity relaxation time is of the same order as the turbulent mixing time scales [24]. It is also noted that the greater dispersion for larger particles is effective only up to a certain number density; the contour levels in Figure 13 are high enough that the greater overall number of particles in the 2- $\mu\text{m}$  simulation dominates.

Figure 14 shows iso-surface plots for the surface-area density, the particle surface area per unit volume, which is indicative of the available surface area for suppression reactions, while Figure 15 shows contours of the same variable in a plane through the SPGG injector centerline. The total surface area available for chemical activity per mass of injected agent increases as the particle size is reduced. If the particulate were evenly distributed, the specific available surface area would be of the order of  $1\text{ m}^{-1}$  (1 square meter of surface per cubic meter of volume) for the 15- $\mu\text{m}$  particles and  $8\text{ m}^{-1}$  for the 2- $\mu\text{m}$  particles, based on the injected mass and the chamber volume. Clearly, there is substantially more surface area available with smaller particles. However, the distribution of area is observed to be more uniform for the larger particles, as previously noted, due to enhanced turbulent dispersion. This increased dispersion is responsible for the greater volume coverage for a surface density of  $1\text{ m}^{-1}$  with larger (15- $\mu\text{m}$ ) particles as shown in Figures 14 and 15.

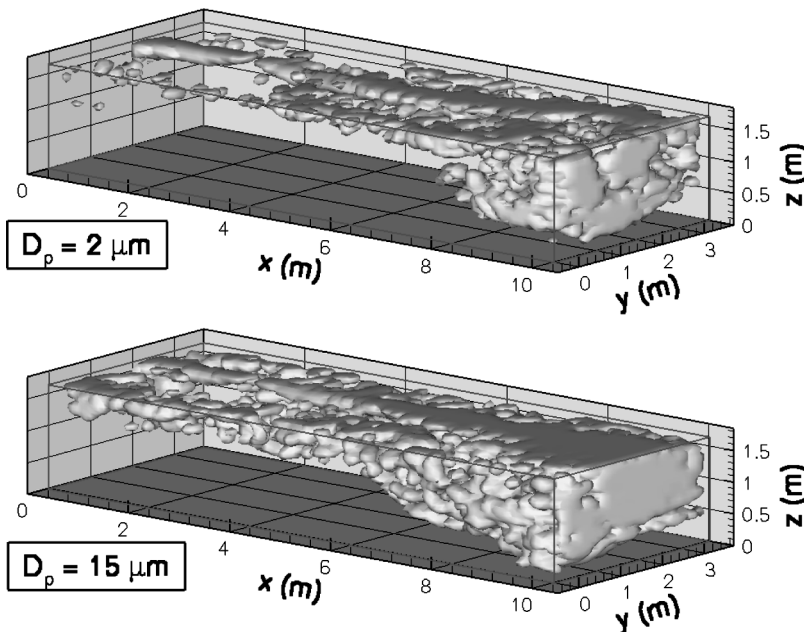
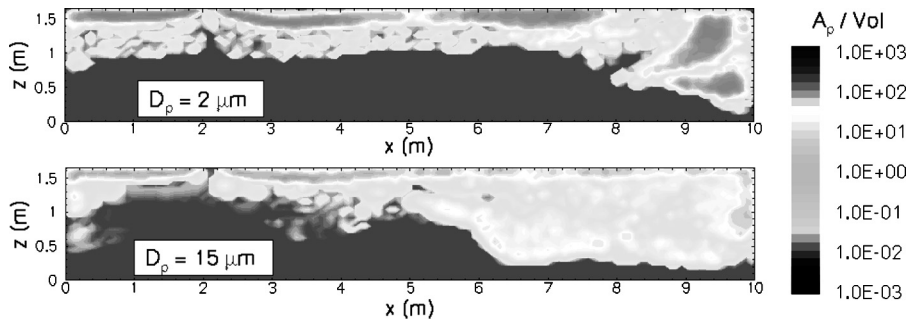


Figure 14. Particle surface area density Iso-surface at  $1.0\text{ m}^{-1}$  for the end of injection (10s).



**Figure 15.** Particle surface area density in the cargo bay at a plane through the SPGG injector centerline at the end of injection (10 s).

## CONCLUSIONS

Several modifications were made to the Vulcan spray modules that were required to simulate various fire-suppression systems. These changes were necessary to improve the robustness and accuracy of the time-splitting integration technique, as well as to allow the efficient solution of very small particles and to improve the consistency of how the two-way coupling source terms are applied to the fluid grid. Ease of use of the code was improved by making these techniques automatic and removing several manual stability tuning parameters from the code input.

For scenarios where the mass momentum and energy associated with the condensed phase is significant, care is required in coupling the gas-phase and condensed-phase conservation equations. Three algorithm improvements allow the proper spray evolution to be predicted. First, the particle evolution subcycling time step is now chosen automatically based on the rate of momentum change from the particles with the shortest time scales and the momentum change associated with the equilibration of the gas and condensed phases. Second, the gas-phase source terms are made equivalent to the condensed-phase source terms to ensure conservation. Third, the gas-phase source terms are distributed over the span of a parcel in a manner that mimics the distribution of these source terms across the parcel.

Two algorithm changes allow the simulation of an increased range of particle sizes, particularly the simulation of small particles. These include the tuning of the particle ODE solver and the development of a novel equilibrium particle method coupled to the SSF model. The equilibrium particle method takes advantage of the separation of time scales to allow an algebraic solution for particle evolution to replace the ODE-based evolution, greatly improving computational efficiency.

Results have been presented that demonstrate the capability of the present Vulcan spray module to simulate the transport of solid particulate KBr and  $K_2CO_3$  particles found in the Goodrich-244 fire-suppressant gases. Separate simulations were conducted using particles of 2- $\mu\text{m}$  and 15- $\mu\text{m}$  diameter, where these sizes were selected based on both measured particle sizes from a test of the SPGG system and the ability of the particles to exercise both the traditional stochastic separated flow solver and the new equilibrium particle solver.

The particle size significantly affects the particle number density and surface area available for chemical activity; smaller particles increase both of these quantities when measured globally (total particles or surface area per cargo bay volume). Particle size also has a significant effect on dispersion, due to the well-known turbulence interaction, whereby intermediate-sized particles can be dispersed more than either very small or very large particles. The result is that the larger (15- $\mu\text{m}$ ) particles were more evenly distributed in the cargo bay than the smaller (2- $\mu\text{m}$ ) particles. The trajectories of larger particles were also found to deviate from that of the carrier gas when turning corners in the cargo bay, leading to a large fraction of these particles adhering to the wall. Smaller particles followed the flow more closely and did not experience this phenomenon to any notable extent. Depending on the number and area density required to suppress the fire, these results could lead to enhanced suppression with either smaller or larger particles.

## REFERENCES

1. D. E. Olander, Development and Testing of Goodrich 233 Fire Suppressant, *Proc. 12th Halon Options Technical Working Conf.*, Albuquerque, NM, April 30–May 2, 2002.
2. P. E. DesJardin and L. A. Gritzo, A Dilute Spray Model for Fire Simulations: Formation, Usage and Benchmark Problems, Sandia Tech. Rep. SAND2002-3419, 2002.
3. S. S. Yoon, J. C. Hewson, P. E. DesJardin, D. J. Glaze, A. R. Black, and R. R. Skaggs, Numerical Modeling and Experimental Measurement of a High Speed Solid-Cone Water Spray for Use in Fire Suppression Applications, *Int. J. Multiphase Flow*, vol. 30, pp. 1369–1750, 2004.
4. W. P. Jones and B. E. Launder, Prediction of Laminarization with a 2-Equation Model of Turbulence. *Int. J. Heat Mass Transfer*, vol. 15, p. 301, 1972.
5. S. V. Patankar, *Numerical Heat Transfer and Fluid Flow*, Taylor & Francis, New York, 1980.
6. G. M. Faeth, Mixing, Transport and Combustion in Sprays, *Prog. Energy Combustion Sci.*, vol. 13, pp. 293–345, 1987.
7. A. A. Amsden, J. D. Ramshaw, P. O'Rourke, and J. K. Dukowicz, KIVA: A Computer Program for Two and Three-Dimensional Fluid Flows with Chemical Reactions and Fuel Sprays. Los Alamos Tech. Rep. LA-10245, 1985.
8. J. F. Wiedenhofer and R. D. Reitz, Modeling the Effect of EGR and Multiple Injection Schemes on I.C. Engine Component Temperatures, *Numer. Heat Transfer A*, vol. 37, pp. 673–694, 2000.
9. A. K. Tolpadi, S. K. Aggarwal, and H. C. Mongia, An Advanced Spray Model for Application to the Prediction of Gas Turbine Combustor Flow Fields, *Numer. Heat Transfer A*, vol. 38, pp. 325–340, 2000.
10. W. K. Chow and B. Yao, Numerical Modeling for Interaction of a Water Spray with Smoke Layer, *Numer. Heat Transfer A*, vol. 39, pp. 267–283, 2001.
11. M. S. Raju, On the Importance of Chemistry/Turbulence Interactions in Spray Computations, *Numer. Heat Transfer B*, vol. 41, pp. 409–432, 2002.
12. J. L. Consalvi, B. Porterie, and J. C. Loraud, On the Use of Gray Assumption for Modeling Thermal Radiation through Water Sprays, *Numer. Heat Transfer A*, vol. 44, pp. 505–519, 2003.
13. S. Roychoudhary and T. L. Bergman, Response of Agglomerated, Multic ceramic Particles to Intense Heating and Cooling for Thermal Plasma Spraying Simulation, *Numer. Heat Transfer A*, vol. 45, pp. 211–233, 2004.

14. W. A. Sirignano, *Fluid Dynamics and Transport of Droplets and Sprays*, Cambridge University Press, New York, 1999.
15. M. R. Maxey and J. J. Riley, Equation of Motion for a Small Rigid Sphere in a Nonuniform Flow, *Phys. Fluids*, vol. 26, pp. 883–889, 1983.
16. F. Odar and W. S. Hamilton, Forces on a Sphere Accelerating in a Viscous Fluid, *J. Fluid Mech.*, vol. 18, pp. 302–314, 1964.
17. C. Crowe, M. Sommerfeld, and Y. Tsuji, *Multiphase Flows with Droplets and Particles*, CRC Press, New York, 1998.
18. S. S. Yoon, H. Y. Kim, J. C. Hewson, J. M. Suo-Anttila, D. J. Glaze, and P. E. DesJardin, A Modeling Investigation of Suppressant Distribution from a Prototype Solid-Propellant Gas-Generator Suppression System into a Simulated Aircraft Cargo Bay, *Drying Technol.*, vol. 25, pp. 1021–1033, 2007.
19. B. J. Lazaro and J. C. Lasheras, Particle Dispersion in a Turbulent, Plane, Free Shear Layer, *Phys. Fluids A*, vol. 6, pp. 1035–1044, 1989.
20. E. Loth, Numerical Approaches for Motion of Dispersed Particles, Droplets, and Bubbles, *Prog. Energy Combustion Sci.*, vol. 26, pp. 161–223, 2000.
21. D. J. Vojir and E. E. Michaelides, Effect of the History Term on the Motion of Rigid Spheres in a Viscous Fluid, *Int. J. Multiphase Flow*, vol. 20, pp. 547–556, 1994.
22. R. P. Chhabra, L. Agarwal, and N. K. Sinha, Drag on Non-spherical Particles: An Evaluation of Available Methods, *Powder Technol.*, vol. 101, pp. 288–295, 1999.
23. G. H. Ganser, A Rational Approach to Drag Prediction of Spherical and Nonspherical Particles, *Powder Technol.*, vol. 77, pp. 143–152, 1993.
24. D. J. Glaze and S. H. Frankel, Stochastic Inlet Conditions for Large Eddy Simulation of a Fully Turbulent Jet, *AIAA J.*, vol. 41, pp. 1064–1073, 2003.